NMR structure of DREAM: Implications for Ca2+-dependent DNA binding and protein dimerization

5 AUTHORS, INCLUDING:

Aswani Valiveti
University of Maryland, College Park
3 PUBLICATIONS **125** CITATIONS

J.B. Ames
University of California, Davis
103 PUBLICATIONS **3,416** CITATIONS

NMR Structure of DREAM: Implications for Ca^{2+}-Dependent DNA Binding and Protein Dimerization[†,‡]

Jacqueline D. Lusin, Murugendra Vanarotti, Congmin Li, Aswani Valiveti,[§] and James B. Ames*

Department of Chemistry, University of California, Davis, California 95616

Received August 24, 2007; Revised Manuscript Received December 14, 2007

ABSTRACT: DREAM (calsenilin/KChIP3) is an EF-hand calcium-binding protein that binds to specific DNA sequences and regulates Ca^{2+}-induced transcription of prodynorphin and c-fos genes. Here, we present the atomic-resolution structure of Ca^{2+}-bound DREAM in solution determined by nuclear magnetic resonance (NMR) spectroscopy. Pulsed-field gradient NMR diffusion experiments and ^{15}N NMR relaxation analysis indicate that Ca^{2+}-bound DREAM forms a stable dimer in solution. The structure of the first 77 residues from the N-terminus could not be determined by our NMR analysis. The C-terminal DREAM structure (residues 78−256) contains four EF-hand motifs arranged in a tandem linear array, similar to that seen in KChIP1, recoverin, and other structures of the neuronal calcium sensor (NCS) branch of the calmodulin superfamily. Mg^{2+} is bound at the second EF-hand, whereas Ca^{2+} is bound functionally at the third and fourth sites. The first and second EF-hands form an exposed hydrophobic groove on the protein surface lined by side-chain atoms of L96, F100, F114, I117, Y118, F121, F122, Y151, L155, L158, and L159 that are highly conserved in all NCS proteins. An exposed leucine near the C-terminus (L251) is suggested to form intermolecular contacts with leucine residues in the hydrophobic groove (L155, L158, and L159). Positively charged side chains of Arg and Lys (Lys87, Lys90, Lys91, Arg98, Lys101, Arg160, and Lys166) are clustered on one side of the protein surface and may mediate electrostatic contacts with DNA targets. We propose that Ca^{2+}-induced dimerization of DREAM may partially block the putative DNA-binding site, which may suggest as to how Ca^{2+} abolishes DREAM binding to DNA to activate the transcription of prodynorphin and other downstream genes in pain control.

DREAM (downstream regulatory element antagonist modulator also known as calsenilin (*1*) and KChIP3[1] (*2*)) is a 29 kDa EF-hand Ca^{2+}-binding protein that serves as a transcriptional repressor for pain modulation (*3−5*). DREAM translocates into the nucleus during calcium signaling (*6*) and blocks the transcription of prodynorphin and c-fos genes by binding to specific DNA sequences (DRE, downstream regulatory element (*7*, *8*)). DRE sequences bind to DREAM only in the Ca^{2+}-free state because Ca^{2+} binding by DREAM induces conformational changes that abolish its ability to bind to DRE (*9−11*). Hence, DREAM is the only known Ca^{2+}-binding protein that binds to specific DNA sequences and directly regulates transcription in a calcium-dependent fashion. DREAM also binds to protein targets (*2*, *12*) and regulates transcription by interacting with nonsteroid nuclear receptors (*13*), leucine zipper proteins (*11*, *14*), and thyroid transcription factor 1 (*15*). The importance of DREAM as a transcriptional regulator is demonstrated in DREAM-deficient mice that exhibit ongoing analgesia due to upregulated transcription of prodynorphin (*16*). The DREAM knockout mice also exhibit mild effects on β-amyloid production and long-term potentiation (*17*) but do not exhibit any motor or behavioral abnormalities. Hence, DREAM regulates pain transmission by controlling prodynorphin expression and represents an attractive therapeutic opportunity for managing pain.

DREAM contains four EF-hand Ca^{2+}-binding motifs (*18*, *19*) and a nonconserved N-terminal region (residues 1−65, Figure 1). The N-terminal extension contains a number of positively charged residues, suggesting initially that this region might form a DNA-binding domain. However, deletion of the N-terminal region does not abolish functional DNA binding (*10*, *14*, *20*) and/or Ca^{2+}-induced protein dimerization (*20*). In addition, DREAM was shown to be a substrate for caspase-3 cleavage at residue 64 (*21*), suggesting a functional role for the proteolytic removal of the N-terminal region inside the cell. Indeed, the N-terminal region is suggested to be structurally unstable in the HSQC spectra of full-length DREAM (Supporting Information Figure 2). Finally, N-terminal deletion constructs of the related KChIP

[1] Abbreviations: Ca^{2+}, calcium ion; Mg^{2+}, magnesium ion; DREAM, downstream regulatory element antagonist modulator; EDTA, ethylenediaminetetraacetic acid; EMSA, electrophoretic mobility shift assay; HMQC, heteronuclear multiple quantum coherence; HSQC, heteronuclear single quantum coherence; IPTG, isopropylthiogalactoside; ITC, isothermal titration calorimetry; KChIP, potassium channel interacting protein; NMR, nuclear magnetic resonance; NOE, nuclear Overhauser effect; NOESY, nuclear Overhauser effect spectroscopy; rmsd, root-mean-squared deviation; SDS-PAGE, sodium dodecylsulfate-polyacrylamide gel electrophoresis; TOCSY, total correlation spectroscopy.

```
                1        10        20        30        40        50        60        70
DREAM      MQRTKEAVKA SDGSLLGDPG RIPLSKRESI KWQRPRFTRQ ALMRCCLIKW ILSSAAPQGS DSSDSELELS
KChIP1     ~~~~~~~~~~ ~~~~~~~~~~ ~~~~~~~~~~ ~~~~~~~~MG AVMG..TFSS LQTKQRRPSK DKIEDELEMT
Frequenin  ~~~~~~~~~~ ~~~~~~~~~~ ~~~~~~~~~~ ~~~~~~~~~~ ~~~~~~~~~~ ~~~~~~~~~~ ~~~~~MG.KK
Recoverin  ~~~~~~~~~~ ~~~~~~~~~~ ~~~~~~~~~~ ~~~~~~~~~~ ~~~~~~~~~~ ~~~~~~~~~~ ~~~~~MGNSK
```

EF1

α1   α2   β1   α3   α4

```
                80        90        100       110       120       130       140
DREAM      TVRHQPEGLD QLQAQTKFTK KELQSLYRGF KNECPTGLVD EDTFKLIYSQ FFPQGDATTY AHFLFNAFDA
KChIP1     MVCHRPEGLE QLEAQTNFTK RELQVLYRGF KNECPSGVVN EDTFKQIYAQ FFPHGDASTY AHYLFNAFDT
Frequenin  SSKLKQDTID RLTTDTYFTE KEIRQWHKGF LKDCPNGLLT EQGFIKIYKQ FFPQGDPSKF ASLVFRVFDE
Recoverin  SGALSKEILE ELQLNTKFTE EELSSWYQSF LKECPSGRIT RQEFQTIYSK FFPEADPKAY AQHVFRSFDA
```

EF2   **EF3**

β2   α5   α6   β3   α7

```
                150       160       170       180       190       200
DREAM      DGNGAIHFED FVVGLSILLR GTVHEKLKWA FNLYDINKDG CITKEEMLAI MKSIYDMMGR HTYPILRED.
KChIP1     TQTGSVKFED FVTALSILLR GTVHEKLRWT FNLYDINKDG YINKEEMMDI VKAIYDMMGK YTYPVLKED.
Frequenin  NNDGSIEFEE FIRALSVTSK GNLDEKLQWA FRLYDVDNDG YITREEMYNI VDAIYQMVG. .Q.QPQSEDE
Recoverin  NSDGTLDFKE YVIALHMTSA GKTNQKLEWA FSLYDVDGNG TISKNEVLEI VTAIFKMISP EDTKHLPEDE
```

EF4

α8   β4   α9   α10

```
                210       220       230       240       250
DREAM      .APLEHVERF FQKMDRNQDG VVTIDEFLET CQKDENIMNS MQLFENVI    256
KChIP1     .TPRQHVDVF FQKMDKNKDG IVTLDEFLES CQEDDNIMRS LQLFQNVM    216
Frequenin  NTPQKRVDKI FDQMDKNHDG KLTLEEFREG SKADPRIVQA LSLGGG      187
Recoverin  NTPEKRAEKI WGFFGKKDDD KLTEKEFIEG TLANKEILRL IQFEPQKVKE KLKEKKL  202
```
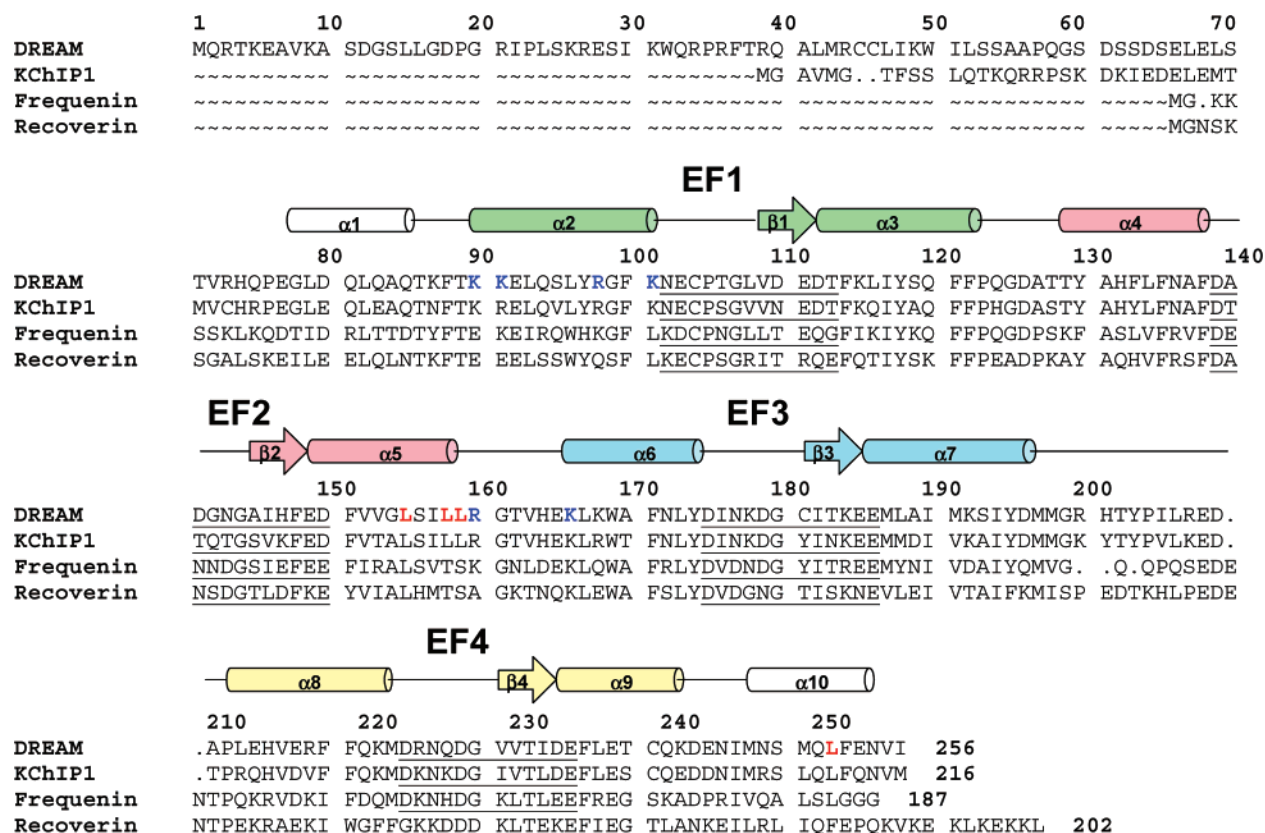
FIGURE 1: Amino acid sequence alignment of mouse DREAM with various NCS proteins. Residues implicated in the dimer interface are highlighted in bold and red. Basic residues suggested for DNA binding are in blue. Secondary structural elements indicated schematically were derived from the analysis of NMR data ($^3J_{HNH\alpha}$, chemical shift index, and sequential NOE patterns shown in Supporting Information Figure 1). The four EF-hands (EF1, EF2, EF3, and EF4) are highlighted in green, red, cyan, and yellow, respectively.

proteins are all fully capable of activating Kv4.2 channels (2).

The four EF-hands of DREAM are more than 45% identical in sequence to KChIP1, recoverin, and related Ca^{2+} sensors of the neuronal calcium sensor (NCS) subclass of the EF-hand superfamily (22, 23) (Figure 1). A characteristic feature of DREAM and the NCS family is the sequence CPXG (Cys104 and Pro105, Figure 1) that prevents the binding of Ca^{2+} to the first EF-hand (EF-1) as seen in the crystal structures of recoverin (24), KChIP1 (25, 26), neurocalcin (27), and frequenin (28). The second EF-hand (EF-2) of DREAM contains aspartate (Asp 150) instead of the usual glutamate at the 12-position of the EF-hand binding loop (Figure 1). The presence of aspartate at the 12-position in other EF-hand proteins is known to diminish binding selectivity for Ca^{2+} versus Mg^{2+} (29). Indeed, Mg^{2+} (and not Ca^{2+}) binds constitutively to DREAM at EF-2 that stabilizes the protein tertiary structure and promotes DNA binding (20). Ca^{2+} binds functionally to the third and fourth EF-hands of DREAM and induces protein dimerization (20).

Three-dimensional structures are now known for many NCS proteins, including KChIP1 (25, 30), recoverin (31, 32), and frequenin (28). These structures are all similar and contain four EF-hands, forming two domains packed in a globular arrangement that contrast with the dumbbell-shaped arrangement of the EF-hand domains seen in calmodulin (33) and troponin C (34). A striking feature of the NCS structures is a solvent-exposed groove lined by hydrophobic residues in the N-terminal domain (F100, F114, I117, Y118, F121,

F122, Y151, and L155) that remains invariant in all other NCS proteins (Figure 1). The exposed hydrophobic residues in GCAP2, recoverin, and KChIP1 have been implicated previously in target recognition (30, 35, 36).

Here, we present the atomic-resolution structure of Ca^{2+}-bound DREAM (residues 65−256) in solution determined by NMR spectroscopy. Ca^{2+}-bound DREAM forms a stable dimeric structure in solution. Residues 65−77 at the N-terminus are structurally disordered, and residues 1−65 are not essential for protein dimerization. The overall main chain structure starting at residue 78 is quite similar to that of KChIP1, recoverin, and other structures of the NCS family. A unique structural feature of DREAM is an exposed C-terminal helix that stabilizes protein dimerization by forming intermolecular contacts with leucine residues in the N-terminal hydrophobic groove. Positively charged side chains of Arg and Lys residues are clustered on one side of the protein surface and may mediate electrostatic contacts with DNA targets. We propose that Ca^{2+}-induced protein dimerization may serve to sterically block the positively charged protein surface, which may suggest as to how Ca^{2+} abolishes DNA binding to DREAM.

EXPERIMENTAL PROCEDURES

Protein Expression and Purification. A deletion construct of mouse DREAM (residues 65−256, originally named DREAM-C (20)) was used throughout this study and was shown previously to exhibit functional binding to DNA and Ca^{2+} (10, 20). The recombinant DREAM-C protein is highly
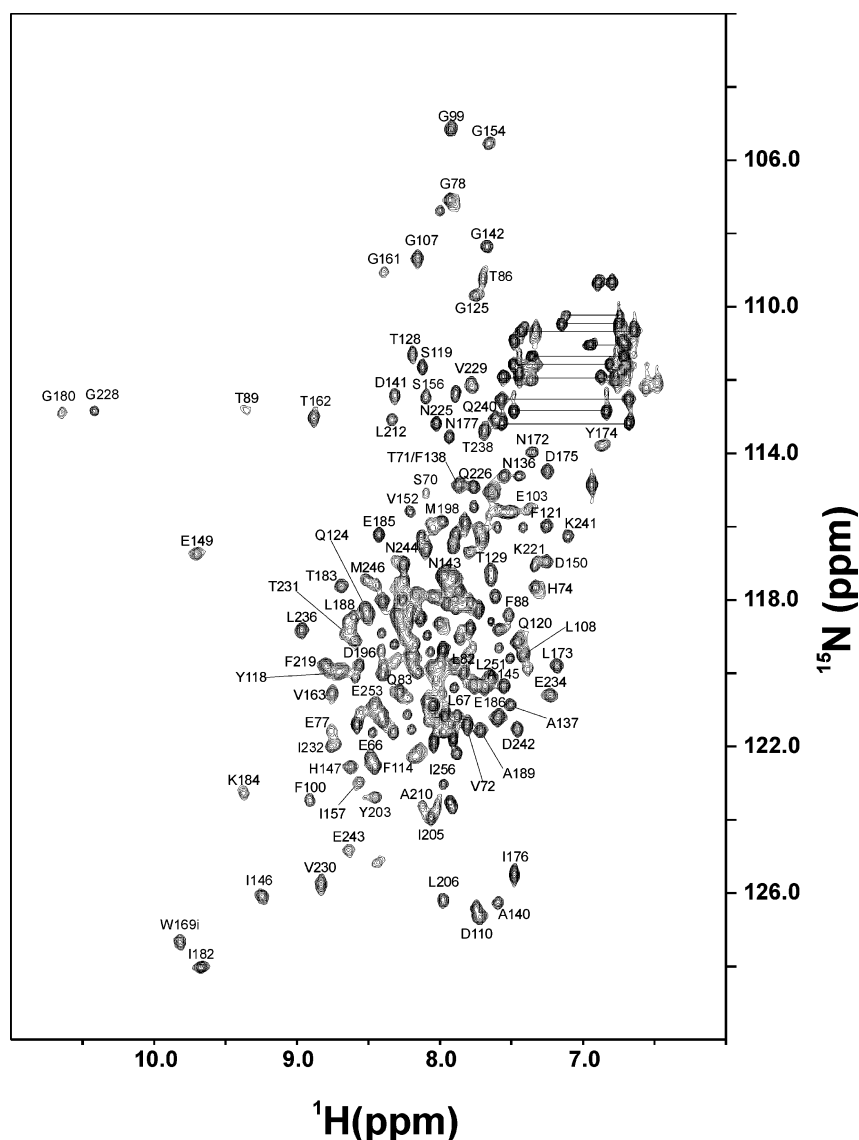
FIGURE 2: $^1H/^{15}N$ HSQC NMR spectrum of DREAM. Peaks corresponding to the NH_2 groups of the side chain amides of Gln and Asn residues are connected by dotted lines. Sequence-specific assignments are indicated.

soluble in bacterial extracts, in contrast to the recombinant full-length protein in which 99% of the protein appeared to be insoluble in inclusion bodies. Gene sequences encoding full-length DREAM, wild-type DREAM-C, and its mutants K90E/K91E, L155A, L158A, L159A, R217E/K221E, and L251A were inserted into pET15b (Novagen) expression vectors. Also, wild-type DREAM-C was inserted into pET42 (Novagen), which codes for the expression of DREAM-C fused to glutathione *S*-transferase (called GST-DREAM). These constructs were transformed into *Escherichia coli* BL21 (DE3) (Stratagene) cells and grown in 2 L of LB medium with 100 μg/mL ampicillin at 37 °C. Recombinant DREAM-C protein expression was induced by adding 0.5 mM IPTG once the cell culture reached an optical density of 0.5 at 600 nm, and the cells were then grown with shaking at 37 °C for 3 h. The full-length DREAM expression was induced by adding 0.2 mM IPTG to a cell culture ($A_{600} = 1.0$) cooled to 15 °C and grown overnight with shaking at 15 °C. Cells were harvested by centrifugation and resuspended in buffer A (20 mM Tris-HCl, pH 8.0, 0.3 M NaCl, 1 mM β-mercaptoethanol, and 20% glycerol) supplemented

with 1 mM phenylmethyl sulfonyl fluoride, 0.2% Tween 20, 20 μg/mL DNase I, and 5 mM $MgCl_2$. Cells were then disrupted by sonication, and soluble protein fractions recovered by centrifugation were applied onto a Ni-loaded Hi-Trap chelating column (or GST-Sepharose Hi-Trap for GST-DREAM) on an ÄKTA purifier (Amersham Biosciences), previously equilibrated with buffer A. After washing with buffer A (until $A_{280} < 0.01$), proteins were eluted with buffer A containing 0.3 M imidazole (or 50 mM reduced glutathione for GST-DREAM). The eluted solution was dialyzed versus buffer B (10 mM Tris-HCl, pH 7.4, 1 mM EDTA, and 1 mM dithiothreitol) for 12 h. The dialyzed sample was applied onto a Hi-Trap DEAE-FF column (Amersham Biosciences) previously equilibrated in buffer B and eluted with a NaCl gradient (0−0.3 M NaCl over 3 h) at a flow rate of 5 mL/min.

The ligand-binding domain (residues 118−427) of the human vitamin D receptor (VDR-6His) was expressed in BL21(DE3)-RIL *E. coli* cells harboring the plasmid, pET28b-VDR-6His, that codes for VDR-6His protein expression. The expressed recombinant protein was purified using the same

procedure described previously for DREAM. Typically, ~0.5 mg of VDR-6His was obtained from a 1 L culture.

Size Exclusion Chromatography. Determination of the molecular weight of Ca^{2+}-bound DREAM and mutants (L251A and L155A) in solution was carried out on a Superdex 200 HR 10/30 column (Amersham) at 4 °C in buffers containing 10 mM Tris-HCl (pH 7.6), 150 mM NaCl, 5 mM $MgCl_2$, 1 mM dithiothreitol, and 5 mM $CaCl_2$. A total of 0.1 mL of various concentrations of protein (0.1−100 μM) was loaded onto the column and eluted at a flow rate of 0.5 mL/min. Apparent molecular weights were calculated using a standard curve of V_e/V_o versus the log of the molecular weights of standard proteins: β-amylase (200 kDa), alcohol dehydrogenase (150 kDa), transferrin (81 kDa), carbonic anhydrase (29 kDa), and myoglobin (17 kDa). V_o is a void volume obtained using blue dextrane (2000 kDa), and V_e is a volume of elution.

Electrophoretic Mobility Shift Assay (EMSA). Synthetic oligonucleotides representing the DRE of human prodynorphin (*9*) were 5′-labeled using the fluorescent dye, Cy5 (Amersham Pharmacia Biotech). The precise nucleotide sequence was 5′-GAAGCCGGAGTCAAGGAGGCCCCTG-3′. Complementary strands were denatured at 95 °C for 10 min and annealed by slowly cooling to room temperature in the presence of 20 mM Tris-HCl, pH 7.6, 10 mM $MgCl_2$, and 0.1 mM EDTA. The formation of double stranded DNA was checked on a 20% nondenaturing polyacrylamide/0.25 × TBE/1% glycerol gel prior to binding. DREAM proteins (wild-type, K90E/K91E, and R217E/K221E) were exchanged into 20 mM Tris-HCl, pH 7.4, 10% glycerol, 100 mM NaCl, 5 mM dithiothreitol, and 0.5 mM EDTA using a PD-10 column and concentrated by Centricon 10 (Millipore) at 4 °C. Protein (0−100 μM, Figure 7) was then incubated with 5 nM Cy5-labeled DNA for 1 h at room temperature in 10 mM HEPES, pH 7.9, 8 mM $MgCl_2$, 0.1 mM EDTA, 2 mM dithiothreitol, 0.05 units of poly(dI-dC) (Amersham Pharmacia Biotech) per milliliter, and with or without 10 mM $CaCl_2$. Protein-DNA complexes were resolved in 5% nondenaturing polyacrylamide/0.25 × TBE/1% glycerol gels at 200 V for 30 min in 0.25 × TBE and 0.5 mM $MgCl_2$ running buffer. Wet fluorescent gels were scanned using the red fluorescence mode of a Storm 860 system (Molecular Dynamics) with a voltage setting of 1000 V and a scanning resolution of 200 μm.

Pull-Down-Binding Assay. A total of 100 μL of Ni-Sepharose resin was equilibrated in batch mode with a 1:1 mixture of VDR-6His and GST-DREAM in the presence and absence of saturating Ca^{2+}. The equilibrated beads were washed twice to remove any excess or unbound GST-DREAM. The washed beads were treated with 10 μL of 1% SDS sample buffer and analyzed using SDS-PAGE.

NMR Spectroscopy. Samples of Ca^{2+}-bound full-length DREAM or DREAM-C (hereafter called DREAM) for NMR analysis consisted of ^{15}N-labeled or ^{13}C/^{15}N-labeled protein (0.5 mM) in 0.3 mL of a 95% H_2O/5% {^{2}H}H_2O solution containing 10 mM Tris-HCl (pH 7.4), 3% glycerol, 30 mM perdeuterated-octylglucoside, 5 mM $MgCl_2$, 5 mM $CaCl_2$, and 1 mM dithiothreitol. The octylglucoside detergent was added to prevent protein aggregation that otherwise occurs slowly over the course of many hours under the conditions of the NMR experiments. All NMR experiments were performed at 37 °C on Bruker Avance 500 or 600 MHz

spectrometers equipped with a four-channel interface and triple-resonance probe with triple-axis pulsed-field gradients. The ^{15}N/^{1}H HSQC spectra (see Figure 2) were recorded on a sample of ^{15}N-labeled DREAM (in 95% H_2O, 5% $^{2}H_2O$). The number of complex points and acquisition times were as follows: 256, 180 ms (^{15}N(F_1)) and and 512, 64 ms (^{1}H-(F_2)). All triple-resonance experiments were performed, processed, and analyzed as described (*37, 38*) on a sample of ^{13}C/^{15}N-labeled DREAM (in 95% H_2O and 5% $^{2}H_2O$) with the following number of complex points and acquisition times: HNCO {^{15}N(F_1) 32, 23.7 ms; ^{13}CO(F_2) 64, 42.7 ms; and ^{1}H(F_3) 512, 64 ms}; HNCACB {^{15}N(F_1) 32, 23.7 ms; ^{13}C(F_2) 48, 6.3 ms; and ^{1}H(F_3) 512, 64 ms}; CBCACONNH {^{15}N(F_1) 32, 23.7 ms; ^{13}C(F_2) 48, 6.3 ms; and ^{1}H(F_3) 512, 64 ms}; and HBHACONNH {^{15}N(F_1) 32, 23.7 ms; ^{1}H$_{ab}$(F_2) 64 21 ms; and ^{1}H(F_3) 512, 64 ms}. ^{15}N-edited and ^{13}C-edited NOESY-HSQC and TOCSY-HSQC experiments were performed as described previously (*39, 40*). The ^{13}C(F_1)-edited, ^{13}C(F_3)-filtered NOESY-HMQC experiments (see Figure 6A) were performed on a sample containing a 1:1 mixture of ^{13}C-labeled and unlabeled protein as described previously (*41*). Stereospecific assignments of chiral methyl groups of valine and leucine were obtained by analyzing ^{1}H/^{13}C HSQC experiments performed on a sample that contained 10% ^{13}C-labeling of DREAM (*42*).

Triple resonance and NOESY spectra measured as stated previously were analyzed to determine resonance assignments and the secondary structure of DREAM. The chemical shift index (see ref *43* for a detailed description of the chemical shift index), $^3J_{NH\alpha}$ coupling constants, and nuclear Overhauser effect (NOE) connectivity patterns for each residue were analyzed and provided a measure of the overall secondary structure. Small $^3J_{NH\alpha}$ coupling constants (<5 Hz), strong NOE connectivities (NN($i,i + 1$) and αN($i,i + 3$)), and a positive chemical shift index are characteristics of residues in an α-helix. Conversely, large $^3J_{NH\alpha}$ coupling constants (>8 Hz), strong αN($i,i + 1$) and weak NN($i,i + 1$) NOE connectivities, and a negative chemical shift index are characteristic of residues in a β-strand. The results of the secondary structure analysis and topology of DREAM are summarized schematically in Supporting Information Figure 1.

^{15}N NMR Relaxation Measurements. ^{15}N T_1, T_2, and ^{15}N-{^{1}H} NOE experiments were performed on Ca^{2+}-bound DREAM at 37 °C using standard pulse sequences described previously (*44*). Longitudinal magnetization decay was recorded using seven different delay times: 0.01, 0.05, 0.15, 0.2, 0.3, 0.4, and 0.8 s. The transverse magnetization decay was recorded with eight different delays: 0.0, 0.016, 0.032, 0.048, 0.064, 0.08, 0.096, and 0.112 s. To check the sample stability, the transverse magnetization decay at 0.032 s was verified unchanged before and after each set of measurements. A recycle delay of 1 s was employed in measurements of both ^{15}N T_1 and T_2 experiments. ^{15}N{^{1}H} NOE values were obtained by recording two sets of spectra in the presence and absence of a 3 s proton saturation period. The NOE experiments were repeated 3 times to calculate the average and standard deviation of the NOE values. Model-free parameters including generalized order parameters and correlation times for internal motion (*45−47*) were determined using the protocol described previously (*48*).

Table 1: Structural Statistics for Ensemble of 15 Calculated Structures of DREAM

NOE restraints (total)	1921
intra ($\|i - j\| = 0$)	729
medium ($1 \leq \|i - j\| \leq 4$)	512
long ($\|i - j\| > 4$)	680
dihedral angle restraints (ϕ and ψ)	228
hydrogen bond restraints in β-sheet regions	158
rmsd from ideal geometry	
bond length (Å)	0.0069 ± 0.00013
bond angles (deg)	2.02 ± 0.0015
Ramachandran plot	
most favored region (%)	82
allowed regions (%)	17
disallowed regions (%)	1
rmsd of atom position from average structure	
β-sheet and α-helical regions (main chain atoms) (Å)	0.70 ± 0.098
β-sheet and α-helical regions (non-hydrogen atoms) (Å)	1.22 ± 0.075

FIGURE 3: Relative intensity of heteronuclear NOE (^{15}N{^{1}H} NOE) plotted as a function of residue number. Error bars are given as the standard deviation of three independent measurements.

Structure Calculation. Backbone and side-chain NMR resonances were assigned as described previously (*38*). Analysis of NOESY data determined nearly 2200 interproton distance relationships throughout the protein (*37*). The NMR-derived distances and dihedral angles then served as constraints (see Table 1) for calculating the three-dimensional structure of the protein using distance geometry and restrained molecular dynamics. Structure calculations were performed using the YASAP protocol within X-PLOR (*49*, *50*), as described previously (*51*). A total of 1921 interproton distance constraints was obtained as described (*38*) by analysis of ^{13}C-edited and ^{15}N-edited NOESY-HSQC spectra (100 ms mixing time) of ^{13}C/^{15}N-labeled DREAM. In addition to the NOE-derived distance constraints, the following additional constraints were included in the structure calculation: 228 dihedral angle constraints (ϕ and ψ); 12 distance constraints involving Ca^{2+} bound to loop residues 1, 3, 5, 7, and 12 in EF-3 and EF-4 (*25*, *33*); and 158 distance constraints for 85 hydrogen bonds verified by identifying slowly exchanging amide protons in hydrogen−deuterium exchange experiments (*52*). Fifty independent structures were calculated, and the 15 structures of lowest energy were selected. The average total and experimental distance energies were 4301 and 203 kcal mol^{-1}. The average root-mean-square (rms) deviations from an idealized geometry for bonds and angles were 0.0069 Å and 2.02°. None of the distance and angle constraints were violated by more than 0.40 Å or 4°, respectively.

The structure of the DREAM dimer was modeled by docking the lowest energy subunit conformer with itself to satisfy intermolecular NOE constraints observed for L155 and L159 with L251 (Figure 6A). The two subunits were positioned so that the respective side-chain Leu methyl groups (with pseudo-atom corrections) were adjusted to be 5 Å apart at the dimer interface. Unfortunately, these distance constraints alone were not sufficient to unambiguously define the entire dimer interface using our simulated annealing procedure performed by X-PLOR. However, the close proximity of L115 (L155) and L211 (L251) at the dimer interface in the X-ray crystal structure of KChIP1 suggested that the KChIP1 dimer interaction may be related to that of DREAM. Therefore, intermolecular interactions involving conserved residues of KChIP1 at the dimer interface were
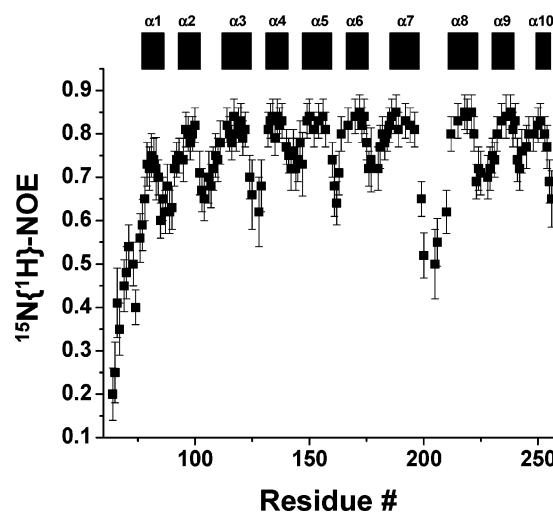
also used initially to help dock the DREAM dimer (KChIP1 residues D202, N204, and R207 with T49, R51, E52, and N54) (*25*). The initially docked DREAM dimer structures generated in this fashion were then subjected to simulated annealing for 25 ps, during which the intermolecular restraints (involving L155 and L159 with L251 and the corresponding invariant KChIP1 residues as stated previously) were ramped on from a force constant of 0−32 kcal/mol Å^2. The resulting dimer structures were then refined by another 25 ps simulated annealing cycle, followed by energy minimization.

RESULTS AND DISCUSSION

NMR Spectral Characterization and Relaxation Analysis. The ^{1}H/^{15}N HSQC NMR spectrum of ^{15}N-labeled Ca^{2+}-bound DREAM exhibited close to the expected number of backbone amide resonances (180 out of 186). The large chemical shift dispersion and uniform peak intensities suggest that the protein is structurally homogeneous and stably folded (Figure 2). Analysis of ^{15}N relaxation parameters (T_1 and T_2) indicates an average rotational correlation time of 18 ± 0.5 ns, suggesting that Ca^{2+}-bound DREAM forms a dimer in solution under NMR conditions, consistent with protein dimerization observed previously (*20*, *25*). Pulsed-field gradient NMR diffusion studies (*53*) and dynamic light scattering analysis also confirmed protein dimerization. Heteronuclear NOE values (^{15}N{^{1}H} NOE) are plotted for each residue in Figure 3. ^{15}N{^{1}H} NOE values less than 0.65 were observed for residues in unstructured regions (residues 65−77 and 198−211). Much higher ^{15}N{^{1}H} NOE values were observed for C-terminal residues in regions of regular secondary structure (residues 78−256), suggesting a rigid main-chain fold, consistent with the compact globular structure determined as follows.

More than 95% of the NMR resonances in the ^{15}N/^{1}H HSQC spectrum were assigned as indicated in Figure 2. NMR chemical shift assignments have been deposited in the BioMagResBank (BMRB) repository (accession no. 15561). NMR assignments were not obtained for residues D126, A127, T202, Y203, E213, and F252 because of weak NMR

intensities perhaps due to chemical exchange broadening. Most of the unassigned residues are in unstructured loop regions, and F252 is predicted to be at the dimer interface. The assigned peaks in the spectrum represent main-chain and side-chain amide groups that serve as fingerprints of the overall conformation. Three-dimensional protein structures derived from the NMR assignments were calculated on the basis of NOE data, slowly exchanging amide NH groups, chemical shift analysis, and $^3J_{NH\alpha}$ spin−spin coupling constants (see Experimental Procedures). The analysis of chemical shift index (CSI) (*54*), $^3J_{NH\alpha}$ (*55*), and hydrogen−deuterium exchange rates of NH groups (*56*) are shown in Supporting Information Figure 1. The final three-dimensional structures of DREAM derived from the NMR data are illustrated in Figures 4 and 5 (atomic coordinates have been deposited in the RCSB Protein Data Bank). Table 1 summarizes the structural statistics calculated for the 15 lowest energy conformers.

The low solubility of full-length DREAM has prevented us from performing its full 3-D NMR structural analysis. However, we were able to obtain a 2-D $^1H/^{15}N$ HSQC spectrum of Ca^{2+}-bound, full-length DREAM (512 scans) and compared it to that of Ca^{2+}-bound DREAM-C (Supporting Information Figure 2). Many amide chemical shifts appear to be identical in these two spectra assigned to the C-terminal residues (65−256), suggesting that the structure of the C-terminal region determined in this study remains fully intact in the full-length protein. The NMR spectrum of the full-length protein contains a number of new peaks not observed in the DREAM-C spectrum that likely represent N-terminal residues (1−64). These additional peaks have a wide range of NMR intensities, caused by exchange broadening perhaps due to structural instability in the N-terminal region. The N-terminal peaks also have amide proton chemical shifts (7.8−8.5 ppm) consistent with a random coil secondary structure. Together, these results suggest that the N-terminal residues (1−64) may be structurally unstable, which would explain as to why these residues are readily cleaved by proteolytic digestion (data not shown and ref *21*) and as to why deletion of these residues has very little impact on both Ca^{2+}-dependent DNA binding and protein dimerization (*10*).

Three-Dimensional Structure of DREAM. The NMR-derived structures of DREAM (residues 78−256) (Figures 4 and 5) revealed an overall fold similar to that of KChIP1 (1.8 Å rmsd for the EF-hand regions) (*25, 30, 57*) and other structures of the NCS family (*27, 28, 31, 58*). The entire polypeptide chain has been defined except for the unstructured N-terminal region (residues 65−77) and loop between EF-3 and EF-4 (residues 198−211). These unstructured regions are poorly defined due to a lack of long-range NOE contacts as well as chemical shift and $^{15}N\{^1H\}$ NOE data indicating an unstructured, random coil secondary structure. The C-terminal structured region of DREAM begins at residue 78 and contains a total of 10 α-helices and four β-strands: α1 (residues 78−85), α2 (residues 90−103), α3 (residues 111−120), α4 (residues 128−138), α5 (residues 148−159), α6 (residues 163−174), α7 (residues 184−198), α8 (residues 211−222), α9 (residues 232−240), and α10 (residues 243−254) and β1 (residues 108−110), β2 (residues 145−147), β3 (residues 161−163), and β4 (residues 229−231) (Figure 1A). DREAM contains two domains comprised
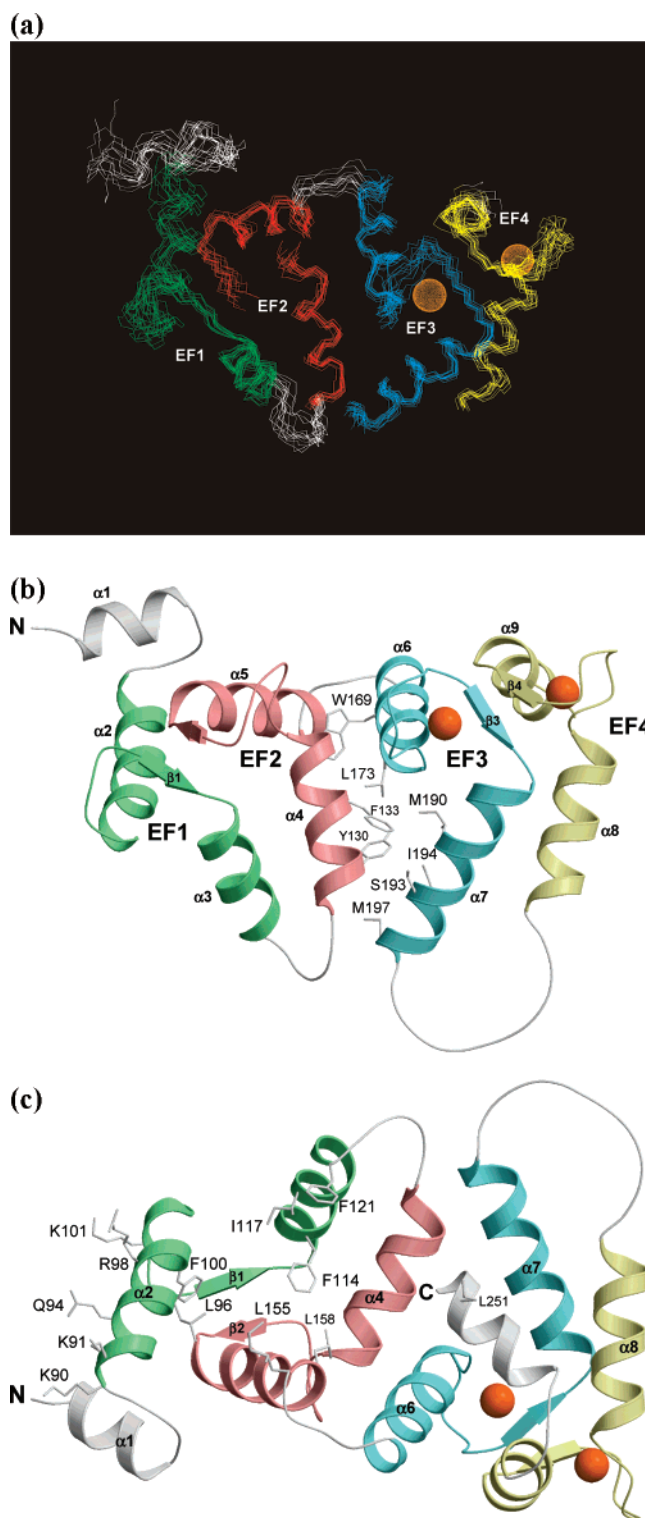

FIGURE 4: Main chain structure of DREAM in solution determined by NMR[2]. (A) Superposition of main chain atoms of 15 lowest energy calculated structures. (B) Ribbon representation of the energy-minimized average main chain structure. (C) 180° rotation of panel A. The N-terminal residues (65−77) and loop between EF-3 and EF-4 (residues 92−97) are unstructured and not shown. EF-hands are highlighted in color as defined in Figure 1. Orange spheres represent bound Ca^{2+}.

of four EF-hands (Figure 1A): EF1 (green, residues 90−119) and EF2 (red, residues 128−157) are linked and form the N-terminal domain; likewise, EF3 (cyan, residues 163−192) and EF4 (yellow, residues 211−240) are linked and
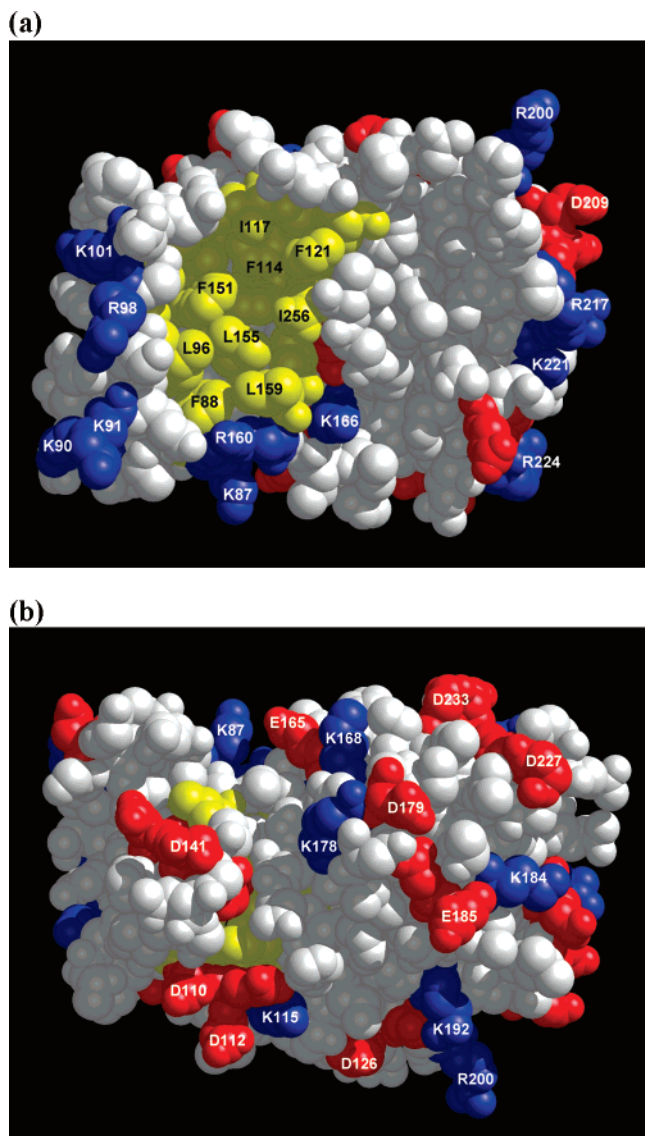
(a)

(b)

FIGURE 5: Space-filling representation of DREAM showing (A) exposed hydrophobic patch and (B) 180° rotation of panel A. Acidic residues (Glu and Asp), basic residues (Lys and Arg), and hydrophobic residues (Leu, Ile, Phe, Trp, and Val) are in red, blue, and yellow, respectively.

form the C-terminal domain. The interface between the two domains is established by interactions between EF2 (Y130, F133, L134, and A137) and EF3 (L173, I190, and M197) that forms a noticeable cleft (see Figure 4A). Each EF-hand consists of a helix−turn−helix structure similar to the structure of Ca^{2+} occupied EF-hands seen in previous structures of calmodulin (*33*), troponin C (*34*), and recoverin (*24*, *31*). The interhelical angles for the EF-hands are 92° (EF-1), 109° (EF-2), 96° (EF-3), and 104° (EF-4). The interhelical angle calculation was performed using the software program Interhlx available at http://structbio.vander-bilt.edu/chazin/wisdom/interhel.html. The four EF-hands are arranged in a tandem array and, overall, form a globular structure with a concave solvent-exposed groove lined by hydrophobic residues (L96, F100, F114, I117, Y118, F121, F122, Y151, L155, L158, and L159; highlighted in yellow in Figure 5A). The C-terminal helix following EF-4 (residues 243−254) forms intramolecular and hydrophobic contacts with a crevice formed between EF-3 (L167, A170, M191,

and L194) and EF-4 (F218, M222, and C239). The C-terminal helix interaction with EF-3 and EF-4 resembles the structural interaction between calmodulin and its M13 target helix (*59*). The C-terminal capping helix of DREAM may prevent adventitious binding of helical target proteins. By contrast, the corresponding C-terminal helix of KChIP1 is displaced far away from the crevice between EF-3 and EF-4, which allows the binding of a target helix from Kv4.3 (*30*). The distinctive disposition of the C-terminal helix in DREAM/KChIP3 versus KChIP1 may help explain some of the apparent functional differences among the various KChIP proteins (*16*, *17*, *60*).

The NMR structure of DREAM was determined under conditions known to cause binding of Mg^{2+} to EF-2 and binding of Ca^{2+} to EF-3 and EF-4 as described previously (*20*). The binding of Mg^{2+} to EF-2 was verified by monitoring Mg^{2+}-dependent amide chemical shift changes (in the presence of saturating Ca^{2+}), which occurred solely for residues in EF-2 (e.g., D141 and G144). Ca^{2+} binding to EF-3 and EF-4 was verified by monitoring characteristic Ca^{2+}-dependent amide chemical shift changes assigned to Gly180 in EF-3 and Gly228 in EF-4 (Figure 2). Unfortunately, the geometry of the coordinate covalent bonds formed between chelating amino acid residues and the bound cations cannot be observed directly in our NMR study. Instead, the stereochemical geometry and chelation of Ca^{2+} bound at EF-3 and EF-4 (orange spheres, Figure 4) was modeled using structural constraints derived from the X-ray structure of KChIP1 (*25*, *30*), which closely resembles the stereochemical binding site structure seen in many other EF-hand proteins and is known to be highly conserved (*18*). In particular, the bound Ca^{2+} is chelated by oxygen atoms from side chains of D175, N177, D179, and E185 for EF-3 and D223, N225, D227, and E233 for EF-4. The stereochemical geometry and chelation of Mg^{2+} bound at EF-2 could not be derived from our NMR analysis and was not modeled in this study. The EF-1 loop in DREAM does not bind Ca^{2+} or Mg^{2+} and is structurally conserved in all other NCS proteins. The structure of the EF-1 loop in DREAM is distorted from a favorable Ca^{2+}-binding geometry by the presence of Pro105 at the fourth position that places a kink in the middle of the loop. Also, the third residue in the loop (Cys104) is not suitable for ligating Ca^{2+}. The bulky sulfhydryl group sterically blocks the entry of Ca^{2+}.

Intermolecular Interactions and Protein Dimerization. Pulsed-field gradient NMR diffusion studies and ^{15}N relaxation analysis both indicated that Ca^{2+}-bound DREAM exists as a dimer under NMR conditions, consistent with our previous hydrodynamic analysis of DREAM dimerization (*20*). Isotope-filtered NOESY experiments (*61*) were performed on a mixed labeled dimer of DREAM (1:1 mixture of ^{13}C-labeled and unlabeled protein) to selectively probe intermolecular contacts at the dimer interface (Figure 6A). The strongest intermonomer NOE intensities were observed between side-chain methyl resonances from leucine residues (at 0.80 and 1.1 ppm). The large number of leucine residues in DREAM and a high degree of chemical shift degeneracy caused ambiguity in assigning all the intermonomer NOEs due to spectral overlap. To help simplify the spectral assignments, we selectively mutated solvent-exposed leucine residues on the surface of the DREAM monomer (L155, L158, L159, and L251 in Figure 5) that likely give rise to
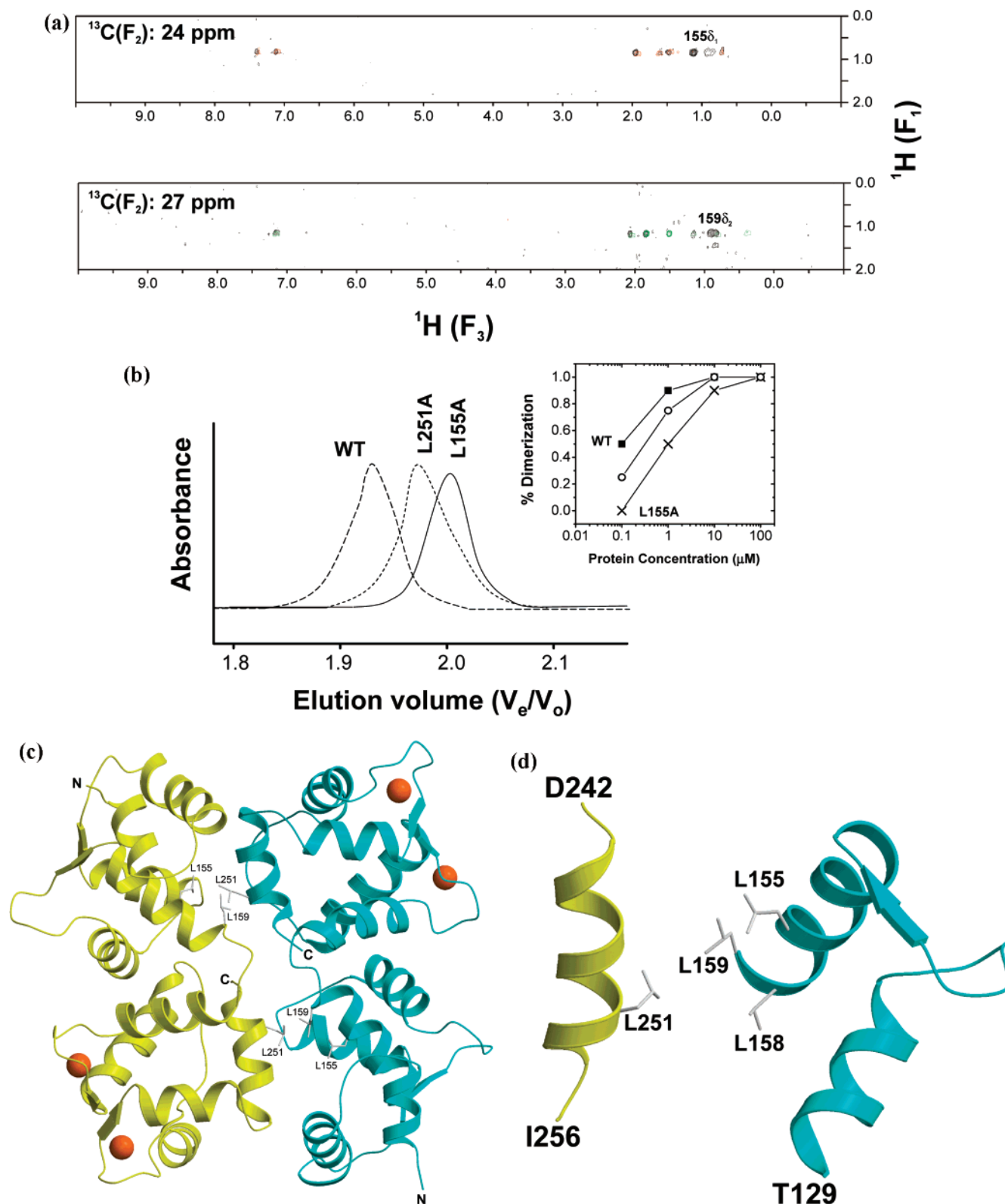
FIGURE 6: Intermolecular interactions within the Ca^{2+}-bound DREAM dimer. (A) ^{13}C(F1)-edited/^{13}C(F3)-filtered NOESY-HMQC spectra of 50% ^{13}C-labeled wild-type DREAM (black), L155A (red), and L159A (green). These spectra yielded information on the individual atoms of DREAM located at the dimer interface: L155, L159, and L251. (B) Size-exclusion chromatography of L155A, L159A, and L251A mutants (at 100 nM protein concentration) and plot of elution time vs protein concentration, indicating at least a 5-fold higher dimerization affinity for the wild-type as compared to each mutant. (C) Modeled three-dimensional structure of the DREAM dimer. (D) Close-up view of the DREAM dimer interface. The dimer structure was calculated by docking the NMR solution structure (Figure 4) such that the side-chain methyl groups of L155 and L159 make the closest possible intermolecular contacts with methyl groups of L251 at the dimer interface (see Experimental Procedures).

the intermonomer NOE intensity in Figure 6A. The single site mutants (L155A, L159A, and L251A) exhibited the largest detectable changes in the NOESY spectra in Figure 6A. Also, the chemical shift assignments for the side-chain

methyl groups of L155 (δ_1: 1.1 ppm), L159 (δ_2: 0.8 ppm), and L251 (δ_1: 1.07 ppm (^{1}H)/27 ppm (^{13}C) and δ_2: 0.8 ppm (^{1}H)/24 ppm (^{13}C)) all match the chemical shifts observed in Figure 6A. The intermonomer NOE cross-peak intensity at 1.1 ppm (^{13}C(F_1) = 24 ppm) was significantly reduced in the spectrum of L155A (red, Figure 6A), and the negative diagonal intensity disappeared in the spectrum of L251A, consistent with the diagonal peak being assigned to its δ_2 methyl group. The off-diagonal peak at 1.1 ppm (^{13}C(F_1) = 24 ppm) is therefore assigned as an intermonomer NOE between the δ_1 methyl of L155 and the δ_2 methyl of L251. The intermonomer cross-peak intensity at 0.8 ppm (^{13}C(F_1) = 27 ppm) was markedly reduced in the spectrum of L159A (green, Figure 6A), suggesting an intermonomer interaction between the δ_2 methyl of L159 and the δ_1 methyl of L251. These observations suggest that the methyl groups of L155 and L159 both form intermolecular contacts with L251.

To further explore as to whether the exposed leucines are important for dimerization, the dimerization affinity was measured for wild-type DREAM and compared to that of the mutants L155A and L251A (Figure 6B). The dimerization dissociation constants were estimated by measuring the elution volume from size exclusion chromatography as a function of protein concentration. At high protein concentrations used for NMR (>100 μM), wild-type DREAM and the two mutants have an elution volume (V_e/V_o = 1.87) that corresponds to a molecular mass of ~50 kDa (dimer). At a low protein concentration (100 nM), L155A has an elution volume (V_e/V_o = 2.02) that corresponds to a molecular mass of ~25 kDa (monomer), whereas the wild-type has an elution volume (V_e/V_o = 1.93) corresponding to a mass of ~38 kDa (halfway between monomer and dimer). The percent of dimerization was estimated by subtracting the observed elution volume from that of the monomer (V_e/V_o = 2.02) and normalizing to the elution volume difference between the monomer and the dimer (2.02 − 1.87 = 0.15). The percent dimerization was then plotted as a function of protein concentration to estimate the dimerization dissociation constant (K_d is the protein concentration at 50% dimerization). The dimerization K_d values for the L155A and L251A mutants were estimated to be 1 μM and 500 nM, respectively, which are ~5-fold weaker than the dimerization affinity estimated for the wild-type (Figure 6B).

The results in Figure 6A,B both support the possibility that exposed leucine residues (L155, L159, and L251) might interact with one another at the protein dimer interface. These exposed leucine residues are also conserved in KChIP1 and play a structural role at the dimer interface in the dimeric X-ray crystal structure (25). The exposed leucine residues (L155, L159, and L251 in Figure 6A) and dimer contacts between invariant residues in the X-ray structure of KChIP1 (see Experimental Procedures) were then used in a docking calculation to generate a modeled structure of the the DREAM protein dimer in Figure 6C. Two polypeptide chains in the dimer were modeled to contact each other in a head-to-tail orientation such that the outer face of the C-terminal helix (L251) fits snugly into the N-terminal hydrophobic groove (near L155 and L159), forming a hydrophobic dimer interface. The exposed leucine residues at the dimer interface (L155, L158, L159, and L251) are conserved in the dimeric DREAM and KChIP1 but are not conserved in monomeric NCS proteins such as recoverin and frequenin (Figure 1).

The leucine residues at the modeled dimer interface of DREAM (L155, L158, and L159) are part of a LxxLL sequence motif in EF-2 that resembles the familiar protein–protein interaction sequence recognized by nonsteroid nuclear receptors and related leucine zipper transcription factor proteins (62). The LxxLL motif is most commonly observed in transcriptional cofactor proteins that interact with hormone-activated nuclear receptors (63). The X-ray crystal structures of nuclear receptors (64, 65) reveal that the LxxLL motifs are found on the surface of an exposed α-helix that forms intermolecular contacts with exposed leucine residues on a target protein. The LxxLL motif in DREAM might similarly promote intermolecular association of DREAM with itself or with nuclear receptor proteins that recognize LxxLL motifs. Indeed, DREAM was shown recently to have a profound affect in promoting Ca^{2+}-induced activation of the vitamin D receptor (13). DREAM also interacts with leucine zipper proteins such as CREB (11) and CREM (14) that contain similar leucine recognition motifs known as leucine-charge residue-rich domains (LCD). Future studies are needed to characterize the atomic-level structural interaction of DREAM bound to transcriptional regulatory proteins (e.g., vitamin D receptor, CREM, and CREB) that recognize LxxLL motifs.

Our modeled structure of the DREAM dimer predicts a head-to-tail interaction, which suggests that both N-terminal (EF-1 and EF-2) and C-terminal (EF-3 and EF-4) domains are required to contact one another to form a high affinity dimer. Therefore, the deletion of either domain would be expected to dramatically weaken or abolish dimer formation. Recently, a fragment of DREAM that comprises only the C-terminal domain (residues 161−256) was synthesized (58), and the structure of the isolated C-domain is nearly identical to what we see for the C-terminal domain in this study (Figure 4). The C-terminal domain fragment forms a low affinity dimer in solution whose dimer dissociation constant is at least 1000-fold weaker than what we measure for wild-type DREAM in Figure 6B. Hence, deletion of the N-terminal domain dramatically lowers the dimerization affinity, consistent with a head-to-tail dimer interaction between the N-terminal and the C-terminal domains as depicted in Figure 6.

Solvent-Exposed Charged Residues Implicated in DNA Binding. Charged amino acid residues in DREAM are unevenly distributed throughout the protein surface (Figure 5). Most striking is the arrangement of K87, K90, K91, R98, K101, R160, and K166, whose side chains form a cluster of positive charge on the protein surface (highlighted in blue in Figure 5A) that flanks the exposed hydrophobic groove (highlighted in yellow in Figure 5A). We propose that this cluster of exposed Arg and Lys residues might represent a potential DNA-binding site. Indeed, many of the exposed, basic residues (K87, K90, K91, and K101) in DREAM are not conserved in NCS proteins such as recoverin and frequenin that lack the ability to bind DNA (Figure 7A). In particular, K90 and K91 in DREAM are both substituted in recoverin by an oppositely charged glutamate. The charge reversing double mutant of DREAM (K90E/K91E) was analyzed to assess as to whether these residues in DREAM form electrostatic contacts with duplex DNA targets called DREs (9). To rule out any nonspecific electrostatic affects due to the decreased overall charge, a different charge
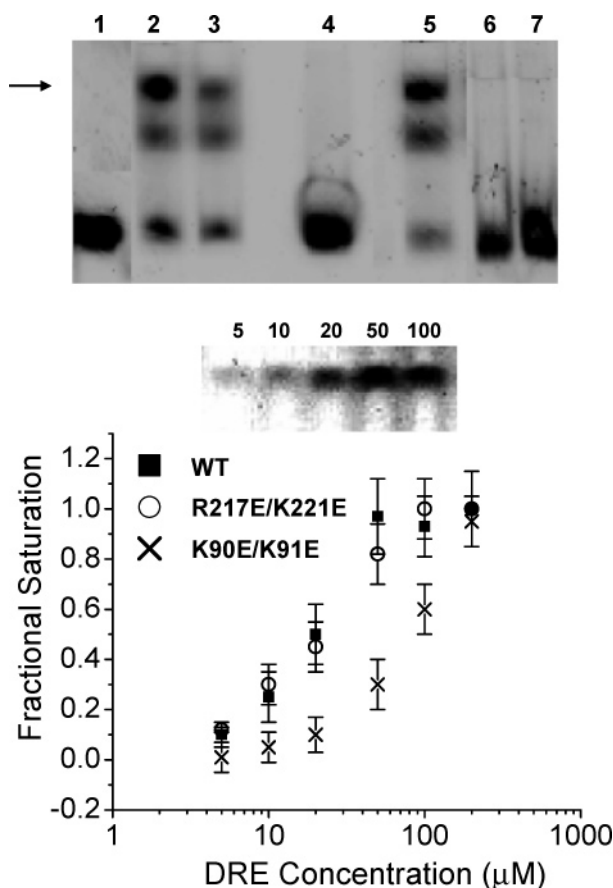
FIGURE 7: Electrophoretic mobility shift assay of DREAM/DRE interaction. In the upper panel, 5 nM Cy5-labeled DRE oligonucleotide was incubated with blank buffer (lane 1), Ca^{2+}-free wild-type DREAM (lane 2), Ca^{2+}-free K90E/K91E (lane 3), Ca^{2+}-bound wild-type (lane 4), Ca^{2+}-free K217E/R221E (lane 5), Ca^{2+}-free recoverin (lane 6), and Ca^{2+}-bound recoverin (lane 7). In the lower panel, Cy5-labeled DRE oligonucleotide was incubated with 0−100 μM Ca^{2+}-free DREAM, and fractional DRE binding is plotted vs protein concentration.

reversing double mutant (R217E/K221E) was also analyzed whose residues are located on the protein surface far away from K90 and K91 (Figure 5A). Electrophoretic mobility shift assays (EMSA) were performed as shown Figure 7 to monitor Ca^{2+}-dependent DRE binding by wild-type, K90E/K91E, and R217E/K221E (positive control). Ca^{2+}-free/Mg^{2+}-bound forms of wild-type, K90E/K91E, and R217E/K221E each bind with fluorescently labeled DRE and form a shifted band (see arrow in upper panel of Figure 7, lanes 2, 3, and 5). The presence of saturating Ca^{2+} abolishes DNA binding to DREAM in each case, and the shifted band disappears (lane 4 in Figure 7). For comparison, recoverin does not bind to DRE in either the presence or the absence of Ca^{2+} (Figure 7, lanes 6− and 7). The decreased intensity of the shifted band for the K90E/K91E mutant as compared to that of the wild-type (Figure 7) suggested a lower binding affinity for this mutant. The affinity of DNA binding to the wild-type and each mutant was estimated by recording the intensity of the EMSA gel shift band at different protein concentrations (lower panel of Figure 7). The fractional binding was estimated from the shifted band intensity plotted as a function of protein concentration. The DNA dissociation constant was then determined as the protein concentration at half saturation. The K90E/K91E double mutant exhibited at least a

3-fold weaker binding to DRE as compared to that of the wild-type, whereas mutation of the remote C-terminal charged residues (R217E/K221E) had almost no effect on the DNA-binding affinity within experimental error (Figure 7). These results suggest a specific role for both K90 and K91 in the DNA-binding site.

Basic side chains (K90, K91, R98, and K101) are all located on the same solvent-exposed face of the entering helix of EF-1 (helix α_2 in Figures 1 and 4B). Hence, the basic entering helix of EF-1 (α_2) in DREAM is somewhat analogous to the basic helix in the familiar basic helix−loop−helix (bHLH) DNA-binding motif, in which exposed residues on the basic helix forms sequence-specific contacts with DNA (*66*). In particular, the exposed basic helix in MyoD contains positively charged side chains (Arg111 and Arg121) that form hydrogen-bonding contacts with heteroatoms of specific nucleotide bases in the major groove of DNA targets. We propose that exposed side-chain groups in DREAM (K90, K91, Q94, R98, and K101) along the basic helix (α_2) may form hydrogen-bonding contacts with heteroatoms from the GTCA sequence (*7, 8*) in the major groove of DRE, analogous to sequence-specific contacts formed by various bHLH DNA-binding proteins (*67*). Future structural studies on Ca^{2+}-free/Mg^{2+}-bound DREAM are needed to test these predictions and to further elucidate the atomic-level structural interactions with DREAM bound to DNA.

Implications for Ca^{2+}-Dependent Transcription. DREAM is a calcium sensing protein in the brain that binds to specific DNA sequences (DRE) and thereby regulates transcription in a calcium-dependent fashion. DREAM was originally discovered to suppress transcription of the prodynorphin gene by binding to DRE at low basal Ca^{2+} levels (*9*). Southwestern analysis has suggested that Ca^{2+}-free DREAM forms a tetramer that binds to DRE (*9*). Ca^{2+} binding by DREAM induces protein conformational changes, leading to dimer formation (Figure 6C) that promotes its dissociation from DRE and causes upregulated transcription of prodynorphin. Our structure of DREAM suggests a possible DNA-binding site on the protein surface (Figure 5A). Many exposed Arg and Lys residues of DREAM (K87, K90, K91, R98, K101, R160, and K166) are clustered together on the surface, forming a positively charged patch that might interact electrostatically with negatively charged DNA. This patch of positive surface charge appears somewhat occluded in the model of Ca^{2+}-bound DREAM dimer (Figure 6) and might explain as to why Ca^{2+}-bound DREAM is prevented from binding to DNA targets (*10*). We propose that the Ca^{2+}-induced dimerization of DREAM might sterically block the DNA-binding site, which would prevent repressor binding to DRE and thereby activate transcription of prodynorphin and c-fos genes at high nuclear Ca^{2+} levels during pain control.

DREAM also activates transcription by interacting with nuclear hormone receptors (*13*) and related leucine zipper transcription factor proteins (*11, 14*). In particular, DREAM regulates calcium-dependent and hormone-activated transcription by the vitamin D receptor (VDR) by increasing VDR activity more than 10-fold at high Ca^{2+} levels (*13*). The L155A mutation in DREAM abolishes the stimulatory affect of DREAM on VDR. Our modeled structure of the Ca^{2+}-bound DREAM dimer suggests that L155 may be important for mediating intermolecular contacts at the protein
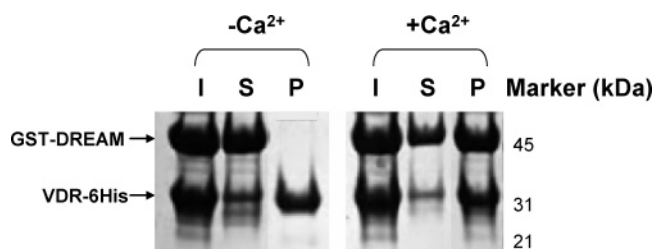
FIGURE 8: SDS-PAGE pull-down assay monitoring Ca^{2+}-dependent binding of GST-DREAM (65−256) to the ligand-binding domain of the vitamin D receptor (VDR-6His) immobilized on Ni-Sepharose beads. I designates input fraction, S designates supernatant, and P designates the pull-down fraction bound to the pellet. Sample buffer was 10 mM Tris-HCl, pH 8.5, 10 nM vitamin D, 1 mM dithiothreitol, 5 mM $MgCl_2$, and ±5 mM $CaCl_2$.

dimer interface (Figure 6D). L155 is also part of an LxxLL sequence motif in EF-2 that is structurally similar to the protein−protein interaction motifs recognized by VDR and other nonsteriod nuclear receptors (*62*). We propose that Ca^{2+}-bound DREAM may bind directly to VDR perhaps similar to the interaction observed previously between Ca^{2+}-free DREAM and related leucine zipper proteins, CREB (*11*) and CREM (*14*). Pull-down assays in Figure 8 now provide evidence in support of a direct Ca^{2+}-induced binding interaction between DREAM and VDR. Ca^{2+}-bound DREAM clearly binds to hormone-activated VDR (but not to the hormone-free receptor). By contrast, Ca^{2+}-free/Mg^{2+}-bound DREAM does not bind to hormone-activated VDR. Preliminary light scattering analysis also confirms that Ca^{2+}-bound DREAM forms a multimeric complex with VDR (data not shown). We suggest that the Ca^{2+}-DREAM/VDR complex may be physiologically important for controlling transcription as a function of both Ca^{2+} and vitamin D. Since the Ca^{2+}-DREAM/VDR complex activates transcription more potently than either VDR alone or VDR/RXR (*13*), this differential activity provides a basis for combinatorial transcriptional control that could integrate both Ca^{2+} and hormone signals during signal transduction. The structural interaction between DREAM and VDR might also provide a molecular basis for the complex interplay between cellular calcium and vitamin D that plays an important role in rickets syndrome and related genetic diseases caused by defects in calcium homeostasis and skeletal metabolism (*68*). Future studies are needed to characterize the atomic-level structural interaction of DREAM bound to VDR and related transcription factor targets.

ACKNOWLEDGMENT

SUPPORTING INFORMATION AVAILABLE

Summary of NMR data and NMR spectrum of full-length DREAM. This material is available free of charge via the Internet at http://pubs.acs.org.

REFERENCES

1. Buxbaum, J. D., Choi, E. K., Luo, Y., Lilliehook, C., Crowley, A. C., Merriam, D. E., and Wasco, W. (1998) Calsenilin: A calcium-binding protein that interacts with the presenilins and regulates the levels of a presenilin fragment, *Nat. Med. 4*, 1177−1181.

2. An, W. F., Bowlby, M. R., Betty, M., Cao, J., Ling, H. P., Mendoza, G., Hinson, J. W., Mattsson, K. I., Strassle, B. W., Trimmer, J. S., and Rhodes, K. J. (2000) Modulation of A-type potassium channels by a family of calcium sensors, *Nature (London, U.K.) 403*, 553−556.

3. Vogt, B. A. (2002) Knocking out the DREAM to study pain, *N. Engl. J. Med. 347*, 362−364.

4. Costigan, M., and Woolf, C. J. (2002) No DREAM, no pain. Closing the spinal gate, *Cell 108*, 297−300.

5. Buxbaum, J. D. (2004) A role for calsenilin and related proteins in multiple aspects of neuronal function, *Biochem. Biophys. Res. Commun. 322*, 1104−1144.

6. Zaidi, N. F., Thomson, E. E., Choi, E. K., Buxbaum, J. D., and Wasco, W. (2004) Intracellular calcium modulates the nuclear translocation of calsenilin, *J. Neurochem. 89*, 593−601.

7. Carrion, A. M., Mellstrom, B., and Naranjo, J. R. (1998) Protein kinase A-dependent derepression of the human prodynorphin gene via differential binding to an intragenic silencer element, *Mol. Cell. Biol. 18*, 6921−6929.

8. Ledo, F., Link, W. A., Carrion, A. M., Echeverria, V., Mellstrom, B., and Naranjo, J. R. (2000) The DREAM-DRE interaction: Key nucleotides and dominant negative mutants, *Biochim. Biophys. Acta 1498*, 162−168.

9. Carrion, A. M., Link, W. A., Ledo, F., Mellstrom, B., and Naranjo, J. R. (1999) DREAM is a Ca^{2+}-regulated transcriptional repressor, *Nature (London, U.K.) 398*, 80−84.

10. Osawa, M., Tong, K. I., Lilliehook, C., Wasco, W., Buxbaum, J. D., Cheng, H. Y., Penninger, J. M., Ikura, M., and Ames, J. B. (2001) Calcium-regulated DNA binding and oligomerization of the neuronal calcium-sensing protein, calsenilin/DREAM/KChIP3, *J. Biol. Chem. 276*, 41005−41013.

11. Ledo, F., Kremer, L., Mellstrom, B., and Naranjo, J. R. (2002) Ca^{2+}-dependent block of CREB-CBP transcription by repressor DREAM, *EMBO J. 21*, 4583−4592.

12. Zaidi, N. F., Kuplast, K. G., Washicosky, K. J., Kajiwara, Y., Buxbaum, J. D., and Wasco, W. (2006) Calsenilin interacts with transcriptional co-repressor C-terminal binding protein(s), *J. Neurochem. 98*, 1290−1301.

13. Scsucova, S., Palacios, D., Savignac, M., Mellstrom, B., Naranjo, J. R., and Ananda, A. (2005) The repressor DREAM acts as a transcriptional activator on Vitamin D and retinoic acid response elements, *Nucleic Acids Res. 33*, 2269−2279.

14. Ledo, F., Carrion, A. M., Link, W. A., Mellstrom, B., and Naranjo, J. R. (2000) DREAM-alphaCREM interaction via leucine-charged domains derepresses downstream regulatory element-dependent transcription, *Mol. Cell. Biol. 20*, 9120−9126.

15. Rivas, M., Mellstrom, B., Naranjo, J. R., and Santisteban, P. (2004) Transcriptional repressor DREAM interacts with thyroid transcription factor-1 and regulates thyroglobulin gene expression, *J. Biol. Chem. 279*, 33114−33122.

16. Cheng, H. Y., Pitcher, G. M., Laviolette, S. R., Whishaw, I. Q., Tong, K. I., Kockeritz, L. K., Wada, T., Joza, N. A., Crackower, M., Goncalves, J., Sarosi, I., Woodgett, J. R., Oliveira, A. J., Ikura, M., Salter, M. W., and Penninger, J. M. (2002) DREAM is a critical transcriptional repressor for pain modulation, *Cell 108*, 31−43.

17. Lilliehook, C., Bozdagi, O., Yao, J., Gomez, M., Zaidi, N. F., Wasco, W., Gandy, S., and Buxbaum, J. D. (2003) Altered Abeta formation and long-term potentiation in a calsenilin knock-out, *J. Neurosci. 23*, 9097−9106.

18. Moncrief, N. D., Kretsinger, R. H., and Goodman, M. (1990) Evolution of EF-hand calcium-modulated proteins, *J. Mol. Evol. 30*, 522−562.

19. Ikura, M. (1996) Calcium binding and conformational response in EF-hand proteins, *Trends Biochem. Sci. 21*, 14−17.

20. Osawa, M., Dace, A., Tong, K. I., Valiveti, A., Ikura, M., and Ames, J. B. (2005) Mg^{2+} and Ca^{2+} differentially regulate DNA binding and dimerization of DREAM, *J. Biol. Chem. 280*, 18008−18014.

21. Choi, E. K., Zaidi, N. F., Miller, J. S., Crowley, A. C., Merriam, D. M., Lilliehook, C., Buxbaum, J. D., and Wasco, W. (2001) Calsenilin is a substrate for caspase-3 that preferentially interacts with the familial Alzheimer's disease-associated C-terminal fragment of presenilin 2, *J. Biol. Chem. 276*, 19197−19204.

22. Ames, J. B., Tanaka, T., Stryer, L., and Ikura, M. (1996) Portrait of a myristoyl switch protein, *Curr. Opin. Struct. Biol. 6*, 432−438.

23. Burgoyne, R. D., and Weiss, J. L. (2001) The neuronal calcium sensor family of Ca^{2+}-binding proteins, *Biochem. J. 353*, 1−12.

24. Flaherty, K. M., Zozulya, S., Stryer, L., and McKay, D. B. (1993) Three-dimensional structure of recoverin, a calcium sensor in vision, *Cell 75*, 709−716.

25. Zhou, W., Qian, Y., Kunjilwar, K., Pfaffinger, P. J., and Choe, S. (2004) Structural insights into the functional interaction of KChIP1 with Shal-type K(+) channels, *Neuron 41*, 573−586.

26. Scannevin, R. H., Wang, K., Jow, F., Megules, J., Kopsco, D. C., Edris, W., Carroll, K. C., Lu, Q., Xu, W., Xu, Z., Katz, A. H., Olland, S., Bowlby, M. R., Chanda, P., and Rhodes, K. J. (2004) Two N-terminal domains of Kv4 K(+) channels regulate binding to and modulation by KChIP1, *Neuron 41*, 587−598.

27. Vijay-Kumar, S., and Kumar, V. D. (1999) Crystal structure of recombinant bovine neurocalcin, *Nat. Struct. Biol. 6*, 80−88.

28. Bourne, Y., Dannenberg, J., Pollmann, V. V., Marchot, P., and Pongs, O. (2001) Immunocytochemical localization and crystal structure of human frequenin (neuronal calcium sensor1), *J. Biol. Chem. 276*, 11949−11955.

29. da Silva, A. C., Kendrick-Jones, J., and Reinach, J. C. (1995) Determinants of ion specificity on EF-hands sites. Conversion of the Ca^{2+}/Mg^{2+} site of smooth muscle myosin regulatory light chain into a $Ca^{(2+)}$-specific site, *J. Biol. Chem. 270*, 6773−6778.

30. Pioletti, M., Findeisen, F., Hura, G. L., and Minor, D. L. (2006) Three-dimensional structure of the KChIP1-Kv4.3 T1 complex reveals a cross-shaped octamer, *Nat. Struct. Mol. Biol. 13*, 987−995.

31. Ames, J. B., Ishima, R., Tanaka, T., Gordon, J. I., Stryer, L., and Ikura, M. (1997) Molecular mechanics of calcium-myristoyl switches, *Nature (London, U.K.) 389*, 198−202.

32. Ames, J. B., Levay, K., Wingard, J. N., Lusin, J. D., and Slepak, V. Z. (2006) Structural basis for calcium-induced inhibition of rhodopsin kinase by recoverin, *J. Biol. Chem. 281*, 37237−37245.

33. Babu, Y. S., Bugg, C. E., and Cook, W. J. (1988) Structure of calmodulin refined at 2.2 Å resolution, *J. Mol. Biol. 204*, 191−204.

34. Herzberg, O., and James, M. N. (1988) Refined crystal structure of troponin C from turkey skeletal muscle at 2.0 Å resolution, *J. Mol. Biol. 203*, 761−779.

35. Ermilov, A. N., Olshevskaya, E. V., and Dizhoor, A. M. (2001) Instead of binding calcium, one of the EF-hand structures in guanylyl cyclase activating protein-2 is required for targeting photoreceptor guanylyl cyclase, *J. Biol. Chem. 276*, 48143−48148.

36. Tachibanaki, S., Nanda, K., Sasaki, K., Ozaki, K., and Kawamura, S. (2000) Amino acid residues of *S*-modulin responsible for interaction with rhodopsin kinase, *J. Biol. Chem. 275*, 3313−3319.

37. Clore, G. M., and Gronenborn, A. M. (1997) NMR structures of proteins and protein complexes beyond 20 000 M(r), *Nat. Struct. Biol. 4*, 849−853.

38. Tanaka, T., Ames, J. B., Kainosho, M., Stryer, L., and Ikura, M. (1998) Differential isotope labeling strategy for determining the structure of myristoylated recoverin by NMR spectroscopy, *J. Biomol. NMR 11*, 135−152.

39. Talluri, S., and Wagner, G. (1996) An optimized 3-D NOESY-HSQC, *J. Magn. Reson., Ser. B 112*, 200−205.

40. Muhandiram, D. R., Farrow, N. A., Xu, G., Smallcombe, S. H., and Kay, L. E. (1993) A gradient NOESY-HSQC experiment for recording NOESY spectra of proteins dissolved in H_2O, *J. Magn. Reson., Ser. B 102*, 317−321.

41. Lee, W., Revington, M. J., Arrowsmith, C., and Kay, L. E. (1994) A pulsed field gradient isotope-filtered 3-D ^{13}C HMQC-NOESY experiment for extracting intermolecular NOE contacts in molecular complexes, *FEBS Lett. 350*, 87−90.

42. Neri, D., Szyperski, T., Otting, G., Senn, H., and Wuthrich, K. (1989) Stereospecific nuclear magnetic resonance assignments of the methyl groups of valine and leucine in the DNA-binding domain of the 434 repressor by biosynthetically directed fractional ^{13}C labeling, *Biochemistry 28*, 7510−7516.

43. Wishart, D. S., Sykes, B. D., and Richards, F. M. (1992) The chemical shift index: A fast and simple method for the assignment of protein secondary structure through NMR spectroscopy, *Biochemistry 31*, 1647−1651.

44. Farrow, N. A., Muhandiram, R., Singer, A. U., Pascal, S. M., Kay, C. M., Gish, G., Shoelson, S. E., Pawson, T., and Kay, L. E. (1994) Backbone dynamics of a free and phosphopeptide-complexed Src

45. homology 2 domain studied by ^{15}N NMR relaxation, *Biochemistry 33*, 5984−6003.

45. Lipari, G., and Szabo, A. (1982) Model-free approach, *J. Am. Chem. Soc. 104*, 4546−4559.

46. Kay, L. E., Torchia, D. A., and Bax, A. (1989) Backbone dynamics of proteins as studied by ^{15}N inverse detected heteronuclear NMR spectroscopy, *Biochemistry 28*, 8972−8979.

47. Mandel, A. M., Akke, M., and Palmer, A. G. (1995) Backbone dynamics of *Escherichia coli* ribonuclease HI: Correlations with structure and function in an active enzyme, *J. Mol. Biol. 246*, 144−163.

48. Freedberg, D. I., Ishima, R., Jacob, J., Wang, Y. X., and Torchia, D. A. (2002) Rapid structural fluctuations of the free HIV protease flaps in solution: Relationship to crystal structures and comparison with predictions of dynamics calculations, *Protein Sci. 11*, 221−232.

49. Brünger, A. T. (1992) *X-PLOR, Version 3.1: A System for X-Ray Crystallography and NMR*, Yale University Press, New Haven, CT.

50. Badger, J., Kumar, R. A., Yip, P., and Szalma, S. (1999) New features and enhancements in the X-PLOR computer program, *Proteins 35*, 25−33.

51. Bagby, S., Harvey, T. S., Eagle, S. G., Inouye, S., and Ikura, M. (1994) NMR-derived three-dimensional solution structure of protein S complexed with calcium, *Structure 2*, 107−122.

52. Ames, J. B., Tanaka, T., Stryer, L., and Ikura, M. (1994) Secondary structure of myristoylated recoverin determined by three-dimensional heteronuclear NMR: Implications for the calcium-myristoyl switch, *Biochemistry 33*, 10743−10753.

53. Altieri, A. S., Hinton, D. P., and Byrd, R. A. (1995) Association of biomolecular systems via pulsed field gradient NMR self-diffusion measurements, *J. Am. Chem. Soc. 117*, 7566−7567.

54. Wishart, D. S., Sykes, B. D., and Richards, F. M. (1991) Relationship between nuclear magnetic resonance chemical shift and protein secondary structure, *J. Mol. Biol. 222*, 311−333.

55. Anglister, J., Grzesiek, S., Wang, A. C., Ren, H., Klee, C. B., and Bax, A. (1994) ^1H, ^{13}C, and ^{15}N nuclear magnetic resonance backbone assignments and secondary structure of human calcineurin B, *Biochemistry 33*, 3540−3547.

56. Wuthrich, K. (1986) *NMR of Proteins and Nucleic Acids*, John Wiley and Sons, Inc., New York.

57. Wang, H., Yan, Y., Liu, Q., Huang, Y., Shen, Y., Chen, L., Chen, Y., and Chai, J. (2007) Structural basis for modulation of Kv4 K^+ channels by auxiliary KChIP subunits, *Nat. Neurosci. 10*, 32−39.

58. Yu, L., Sun, C., Mendoza, R., Wang, J., Matayoshi, E. D., Hebert, E., Pereda, A., Hajduk, P. J., and Olejniczak, E. T. (2007) Solution structure and calcium-binding properties of EF-hands 3 and 4 of calsenilin, *Protein Sci. 16*, 2502−2509.

59. Ikura, M., Clore, G. M., Gronenborn, A. M., Zhu, G., Klee, C. B., and Bax, A. (1992) Solution structure of a calmodulin-target peptide complex by multidimensional NMR, *Science (Washington, DC, U.S.) 256*, 632−638.

60. Kuo, H. C., Cheng, C. F., Clark, R. B., Lin, J. J., Lin, J. L., Hoshijima, M., Nguyen, V. T., Gu, Y., Ikeda, Y., Chu, P. H., Ross, J., Giles, W. R., and Chien, K. R. (2001) A defect in the Kv channel-interacting protein 2 (KChIP2) gene leads to a complete loss of I(to) and confers susceptibility to ventricular tachycardia, *Cell 107*, 801−813.

61. Lee, W., Harvey, T. S., Yin, Y., Yau, P., Litchfield, D., and Arrowsmith, C. H. (1994) Solution structure of the tetrameric minimum transforming domain of p53, *Nat. Struct. Biol. 1*, 877−890.

62. Plevin, M. J., Mills, M. M., and Ikura, M. (2005) The LxxLL motif: A multifunctional binding sequence in transcriptional regulation, *Trends Biochem. Sci. 30*, 66−69.

63. Heery, D. M., Kalkhoven, E., Hoare, S., and Parker, M. G. (1997) A signature motif in transcriptional co-activators mediates binding to nuclear receptors, *Nature (London, U.K.) 387*, 733−736.

64. Nolte, R. T., Wisely, G. B., Westin, S., Cobb, J. E., Lambert, M. H., Kurokawa, R., Rosenfeld, M. G., Willson, T. M., Glass, C. K., and Milburn, M. V. (1998) Ligand binding and co-activator assembly of the peroxisome proliferator-activated receptor-γ, *Nature (London, U.K.) 395*, 137−143.

65. Shiau, A. K., Barstad, D., Loria, P. M., Cheng, L., Kushner, P. J., Agard, D. A., and Greene, G. L. (1998) The structural basis of estrogen receptor/coactivator recognition and the antagonism of this interaction by tamoxifen, *Cell 95*, 927−937.

66. Ma, P. C., Rould, M. A., Weintraub, H., and Pabo, C. O. (1994) Crystal structure of MyoD bHLH domain-DNA complex: Perspectives on DNA recognition and implications for transcriptional activation, *Cell 77*, 451−459.

67. Shimizu, T., Toumoto, A., Ihara, K., Shimizu, M., Kyogoku, Y., Ogawa, N., Oshima, Y., and Hakoshima, T. (1997) Crystal structure of PHO4 bHLH domain-DNA complex: Flanking base recognition, *EMBO J. 16*, 4689−4697.

68. Panda, D. K., Miao, D., Tremblay, M. L., Sirois, J., Farookhi, R., Hendy, G. N., and Goltzman, D. (2001) Targeted ablation of the 25-hydroxyvitamin D 1α-hydroxylase enzyme: Evidence for skeletal, reproductive, and immune dysfunction, *Proc. Natl. Acad. Sci U.S.A. 98*, 7498−7503.